# Extension of sound field reconstruction based on element radiation superposition method in a sparsity framework

Yuan Gao(高塬)[3], Bo-Quan Yang(杨博全)[1,2,3], Sheng-Guo Shi(时胜国)[3], and Hao-Yang Zhang(张昊阳)[1,2,3,†]

[1] *National Key Laboratory of Underwater Acoustic Technology, Harbin Engineering University, Harbin* 150001, *China*
[2] *Key Laboratory of Marine Information Acquisition and Security (Harbin Engineering University), Ministry of Industry and Information Technology, Harbin* 150001, *China*
[3] *College of Underwater Acoustic Engineering, Harbin Engineering University, Harbin* 150001, *China*

(Received 4 June 2022; revised manuscript received 6 August 2022; accepted manuscript online 1 September 2022)

Nearfield acoustic holography (NAH) is a powerful tool for realizing source identification and sound field reconstruction. The wave superposition (WS)-based NAH is appropriate for the spatially extended sources and does not require the complex numerical integrals. Equivalent source method (ESM), as a classical WS approach, is widely used due to its simplicity and efficiency. In the ESM, a virtual source surface is introduced, on which the virtual point sources are taken as the assumed sources, and an optimal retreat distance needs to be considered. A newly proposed WS-based approach, the element radiation superposition method (ERSM), uses piston surface source as the assumed source with no need to choose a virtual source surface. To satisfy the application conditions of piston pressure formula, the sizes of pistons are assumed to be as small as possible, which results in a large number of pistons and sampling points. In this paper, transfer matrix modes (TMMs), which are composed of the singular vectors of the vibro-acoustic transfer matrix, are used as the sparse basis of piston normal velocities. Then, the compressive ERSM based on TMMs is proposed. Compared with the conventional ERSM, the proposed method maintains a good pressure reconstruction when the number of sampling points and pistons are both reduced. Besides, the proposed method is compared with the compressive ESM in a mathematical sense. Both simulations and experiments for a rectangular plate demonstrate the advantage of the proposed method over the existing methods.

**Keywords:** sound field reconstruction, nearfield acoustic holography, element radiation superposition method, sparsity framework

**PACS:** 43.60.Sx, 43.40.+s, 43.60.Pt **DOI:** 10.1088/1674-1056/ac8e55

## 1. Introduction

Nearfield acoustic holography (NAH) is an advanced tool for identifying sound sources and visualizing a sound field. The early NAH was carried out via a spatial Fourier transform and it achieved success in analyzing sources of planar, cylindrical, and spherical shapes.[1–3] Next, the NAH based on inverse boundary element method (IBEM) was suggested for reconstructing arbitrarily shaped sources.[4–6] However, the implementation of IBEM is a challenge because of the demand for excessive sampling points and the awful computation efficiency. The wave superposition (WS) approaches[7–15] are appropriate for the arbitrarily shaped sources and do not require the complex numerical implementation, in which the Helmholtz equation least squares (HELS) method was first suggested as an alternative to the Fourier transform and IBEM approaches.[9,10] The HELS method is formulated by using the field representation based on spherical harmonics, and thus the reconstruction accuracy on a non-spherical surface may be unsatisfactory.[2] Another WS approach, the equivalent source method (ESM), was widely applied to NAH for its simplicity, efficiency, and flexibility.[11–13] Reconstruction using ESM can make satisfactory accuracy with careful choice of parameters, in which the most confusing one is the optimal retreat distance between the actual source surface and the virtual source surface.[14] For continuous sources, singularity problem will arise if the retreat distance is zero or too small, whereas an overly large retreat distance makes inverse reconstruction very ill-conditioned. Moreover, the microphone array should be placed at a location very close to the actual source surface for less ill-posedness of transfer matrix. In some cases, measurements at large hologram distance are needed.[15]

Based on the principle of WS, there is no strict restriction on the style of the assumed sources. Recently, a new NAH technique based on the element radiation superposition method (ERSM) was proposed for spatially extended sources. The theoretical justification of ERSM was given first by Wang *et al.*[16] Then, ERSM applied to NAH was first suggested by Shi *et al.*[17] In ERSM, the actual source surface is divided into regular-shaped pistons (surface sources), and the total sound field is regarded as the superposition of the responses radiated by the pistons. The ERSM is directly derived from the Helmholtz integral equation, and a Fraunhofer approximation is used to construct the transfer matrix. The values in transfer matrix can be fast calculated via the far field pressures exerted by rectangular planar, cylindrical curved or spherical curved

†Corresponding author. E-mail: zhanghaoyang@hrbeu.edu.cn
© 2023 Chinese Physical Society and IOP Publishing Ltd

baffled pistons. The normal velocity on actual source surface is directly obtained as an acoustic quantity via inverse calculation with no need to choose a virtual source surface. Besides, as an approximation of the IBEM, the ERSM avoids the complex numerical integration, and it is immune to the singularity and nonuniqueness difficulties. Shi *et al.*[17] not only proved that the ERSM provides high accuracy in sound field prediction of rectangular plate within nearfield, but also compared the ERSM with ESM in the sound field reconstruction of rectangular plate by using regular sampling. To satisfy the application conditions of the far field approximation, the sizes of pistons are assumed to be as small as possible. Therefore, the number of pistons may be large, which further results in a large number of sampling points.

Since 2012, a number of methods based on the principles of compressive sensing (CS) have been proposed to solve the limitation of the Nyquist criterion. Chardon *et al.*[18] first introduced the concept of CS into NAH. Fernandez *et al.*[19] presented a compressive ESM (CESM), which is suitable for spatially compact sources. Then, Fernandez and Grande[20] applied the block-sparse regularization to the CESM for spatially extended sources. The compressed modal ESM proposed by Bi *et al.*[21] is also applicable to spatially extended sources since the power radiation modes (PRMs) are used as the sparse basis. Bi *et al.*[22] subsequently applied the sparse regularization to the IBEM by introducing the acoustic radiation modes (ARMs). Hu *et al.*[23] proposed a singular value decomposition-based CESM (SVD-CESM) to further improve the reconstruction for spatially extended sources, in which the sparse basis is composed of the transfer matrix modes (TMMs). Hald[24] compared above-mentioned methods and discussed the physical sense of several sparse bases.

In this paper, the TMMs, which are composed of the singular vectors of the vibro-acoustic transfer matrix, are used as the sparse basis of normal velocities of pistons. Based on this sparse basis, the compressive ERSM is proposed. Compared with the conventional ERSM, the proposed method maintains a good pressure reconstruction when the number of sampling points and pistons are both reduced. Besides, the proposed method possesses less ill-posedness in reconstruction than SVD-CESM, and thus it provides higher accuracy. The remainder of this paper is organized as follows. In Section 2, an overview of the ERSM-based NAH in the least-square is provided, and then the proposed method is described. Sections 3 and 4 give the simulations and experiments for a rectangular plate, respectively, in which the proposed method is compared with the conventional ERSM and SVD-CESM. In Section 5, conclusions are drawn.

## 2. Theoretical background

### 2.1. Theory of the ERSM

We consider an arbitrarily-shaped spatially extended source placed in an infinite and homogeneous lossless fluid, and its generated sound field can be calculated by using the Helmholtz integral formulation. Dividing the source surface into small elements, the pressure $p$ at any field point $\boldsymbol{r}$ can be expressed in a matrix form as

$$p(\boldsymbol{r}) = [\boldsymbol{A}]_{1\times N}[\boldsymbol{p}_{\mathrm{S}}]_{N\times 1} + [\boldsymbol{B}]_{1\times N}[\boldsymbol{v}_{\mathrm{S}}]_{N\times 1}, \tag{1}$$

where $N$ is the number of discretized elements on the source surface, $[\cdot]_{1\times N}$ and $[\cdot]_{N\times 1}$ each denote the dimension of a matrix or vector, $\boldsymbol{p}_{\mathrm{S}}$ is the pressure on the source surface, $\boldsymbol{v}_{\mathrm{S}}$ is the normal velocity on the source surface, and $\boldsymbol{A}$ and $\boldsymbol{B}$ only depend on the frequency and the shape of the source surface.[16] Furthermore, according to the surface Helmholtz integral formulation, an equation relating $\boldsymbol{p}_{\mathrm{S}}$ and $\boldsymbol{v}_{\mathrm{S}}$ is obtained as

$$[\boldsymbol{C}]_{N\times N}[\boldsymbol{p}_{\mathrm{S}}]_{N\times 1} = [\boldsymbol{D}]_{N\times N}[\boldsymbol{v}_{\mathrm{S}}]_{N\times 1}, \tag{2}$$

where the matrices $\boldsymbol{C}$ and $\boldsymbol{D}$ also depend on the frequency and the source geometry.[16] After equation (2) is multiplied the inverse matrix of $\boldsymbol{C}$, it turns into the following form:

$$\boldsymbol{p}_{\mathrm{S}} = \boldsymbol{C}^{-1}\boldsymbol{D}\boldsymbol{v}_{\mathrm{S}} = [\boldsymbol{Z}]_{N\times N}\boldsymbol{v}_{\mathrm{S}}, \tag{3}$$

where $\boldsymbol{Z}$ is the acoustic impedance matrix of the source surface. Combining Eq. (1) with Eq. (3), the pressure $p$ is expressed as

$$p(\boldsymbol{r}) = (\boldsymbol{A}\boldsymbol{Z} + \boldsymbol{B})\boldsymbol{v}_{\mathrm{S}} = [\boldsymbol{G}]_{1\times N}\boldsymbol{v}_{\mathrm{S}}. \tag{4}$$

Equation (4) is also a standard formula in IBEM, and the $\boldsymbol{G}$ is calculated via complex numerical integrals in IBEM.[22] Here, based on the principle of ERSM, the transfer function $\boldsymbol{G} = [G_1,\ G_2,\ \ldots,\ G_N]$ is seen as a weighting matrix, and the pressure $p$ is the superposition of the responses produced by discretized elements. Remarkably, the discretization is performed on the actual source surface with no need to set the virtual sources, and the acoustic quantity is the normal velocity instead of the source intensity, which is the important difference between the ERSM method and other WS-based methods. To distinguish from other transfer functions, the $\boldsymbol{G}$ is rewritten as $\boldsymbol{G}_{\mathrm{vat}}$, which means the vibro-acoustic transfer function. It is supposed that only the first discretized element vibrates at unit velocity and other elements remain stationary, *i.e.*, $\boldsymbol{v}_{\mathrm{S}} = [1,0,\ldots,0]^{\mathrm{T}}$. Substituting $\boldsymbol{v}_{\mathrm{S}}$ into Eq. (4) gives $G_1 = p_1$. If $\boldsymbol{v}_{\mathrm{S}} = [0,1,0,\ldots,0]^{\mathrm{T}}$, substituting this into Eq. (4) presents $G_2 = p_2$. Likewise, the usual result is that $G_i = p_i$ $(i = 1,2,\ldots,N)$, and hence $\boldsymbol{G}_{\mathrm{vat}}$ is expressed as

$$\boldsymbol{G}_{\mathrm{vat}} = [p_1, p_2, \ldots, p_N], \tag{5}$$

where $p_i$ is the pressure produced by the $i$-th discretized element vibrating at unit velocity. The spatially extended source can be treated as a rigid baffle, and the discretized elements are then modeled as small pistons vibrating uniformly in an infinite rigid baffle. The pressures produced by regular-shaped (*e.g.*, rectangular planar, cylindrically curved, or spherically curved) pistons in a rigid baffle can be calculated by using specific analytical formulas. Figure 1 shows a rectangular planar piston mounted in corresponding infinite rigid baffle. The pressure produced by rectangular planar piston can be expressed as[16,17,25]

$$p(R,\theta,\phi) = \frac{-2\mathrm{j}\rho ckvL_xL_y\,\mathrm{e}^{\mathrm{j}kR}}{\pi R}\mathrm{sinc}\left(kL_x\cos\theta\cos\phi\right) \times \mathrm{sinc}\left(kL_y\cos\theta\sin\phi\right), \tag{6}$$

where $R$, $\theta$, and $\phi$ denote the distance, elevation, and azimuth, respectively, between a field point and the center of the piston; $L_x$ and $L_y$ are the length and width of the piston, respectively; j is the imaginary unit; $\rho$ is the mass density of the medium; $c$ is the sound speed in the medium; $k$ is the wave number; $v$ is the normal velocity of the piston; $\mathrm{sinc}(\mu) \equiv \sin(\mu)/\mu$.

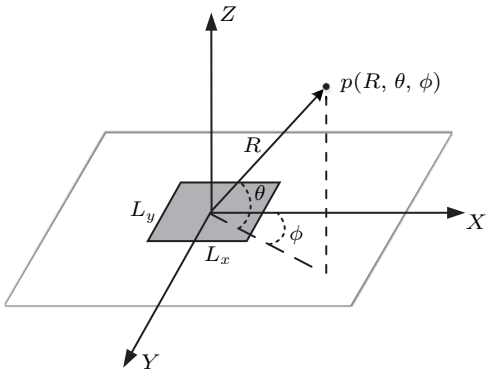



**Fig. 1.** Rectangular planar piston mounted in corresponding rigid baffle.

For plate-like sources, the values in $\boldsymbol{G}_{\mathrm{vat}}$ are fast calculated via Eq. (6), which avoids time-consuming numerical integrals. Equation (6) is of a Fraunhofer approximation, and it requires that $R \gg L_x^2/4\lambda$, in which $\lambda = c/f$ is the acoustic wavelength.[25] $L_x^2/4\lambda$ denotes the distance from the near-field transition to the far-field transition of the piston. Thus equation (6) is the exact analytical solution for the produced pressure in the far field of the piston, but it may result in errors for calculations in the near field of the piston. According to practical requirements, the calculation accuracy and applicable distance can be adjusted by changing the size of the pistons. For unclosed spatially extended sources, it should be noted that the pressures produced by the pistons at the edges of the source surface may also have errors. Nevertheless, for the whole extended source, the pressure $p(\boldsymbol{r})$ will be accurate when most of the values in $\boldsymbol{G}_{\mathrm{vat}}$ are precise. Previous results well show that the ERSM maintains high calculation accuracy from the transition distance to the far field of the piston.[17] In this study, the piston length is set to $L_x < 0.12\lambda_{\min}$ ($\lambda_{\min}$ is the minimum wavelength of the applied frequency band), and all the distance-parameters satisfy the applicable scope of Eq. (6).

### 2.2. ERSM-based NAH

Given that there are $M$ measurement points on the hologram surface, the measured pressures can be expressed in matrix form as

$$\boldsymbol{p}_{\mathrm{H}} = \boldsymbol{G}_{\mathrm{vat}}(\boldsymbol{r}_{\mathrm{H}},\boldsymbol{r}_{\mathrm{S}})\,\boldsymbol{v}_{\mathrm{S}}, \tag{7}$$

where $\boldsymbol{p}_{\mathrm{H}} = [p(\boldsymbol{r}_{\mathrm{H1}}), p(\boldsymbol{r}_{\mathrm{H2}}), \ldots, p(\boldsymbol{r}_{\mathrm{H}M})]^{\mathrm{T}}$ is a column vector that contains the pressures at the $M$ measurement points; $\boldsymbol{r}_{\mathrm{H}m}$ denotes the location of the $m$-th measurement point; $\boldsymbol{v}_{\mathrm{S}} = [v(\boldsymbol{r}_{\mathrm{S1}}), v(\boldsymbol{r}_{\mathrm{S2}}), \ldots, v(\boldsymbol{r}_{\mathrm{S}N})]^{\mathrm{T}}$ is a column vector that contains the normal velocities of the pistons; $N$ is the number of the pistons; $\boldsymbol{r}_{\mathrm{S}n}$ denotes the center location of the $n$-th piston; and $\boldsymbol{G}_{\mathrm{vat}}(\boldsymbol{r}_{\mathrm{H}},\boldsymbol{r}_{\mathrm{S}})$ is the vibro-acoustic transfer matrix relating the pistons to the measurement points, and this can be expressed as

$$\boldsymbol{G}_{\mathrm{vat}}(\boldsymbol{r}_{\mathrm{H}},\boldsymbol{r}_{\mathrm{S}}) = \begin{bmatrix} G_{\mathrm{vat}}(\boldsymbol{r}_{\mathrm{H1}},\boldsymbol{r}_{\mathrm{S1}}) & G_{\mathrm{vat}}(\boldsymbol{r}_{\mathrm{H1}},\boldsymbol{r}_{\mathrm{S2}}) & \cdots & G_{\mathrm{vat}}(\boldsymbol{r}_{\mathrm{H2}},\boldsymbol{r}_{\mathrm{S}N}) \\ G_{\mathrm{vat}}(\boldsymbol{r}_{\mathrm{H2}},\boldsymbol{r}_{\mathrm{S1}}) & G_{\mathrm{vat}}(\boldsymbol{r}_{\mathrm{H2}},\boldsymbol{r}_{\mathrm{S2}}) & \cdots & G_{\mathrm{vat}}(\boldsymbol{r}_{\mathrm{H1}},\boldsymbol{r}_{\mathrm{S}N}) \\ \vdots & \vdots & \cdots & \vdots \\ G_{\mathrm{vat}}(\boldsymbol{r}_{\mathrm{H}M},\boldsymbol{r}_{\mathrm{S1}}) & G_{\mathrm{vat}}(\boldsymbol{r}_{\mathrm{H}M},\boldsymbol{r}_{\mathrm{S2}}) & \cdots & G_{\mathrm{vat}}(\boldsymbol{r}_{\mathrm{H}M},\boldsymbol{r}_{\mathrm{S}N}) \end{bmatrix}. \tag{8}$$

The estimation of $\boldsymbol{v}_{\mathrm{S}}$ from $\boldsymbol{p}_{\mathrm{H}}$ is an inverse problem, which is mathematically ill-posed. For the discrete ill-posed problem, the Tikhonov regularization is introduced, and then equation (7) can be solved in a least square sense through the minimization problem

$$\arg\min_{\boldsymbol{v}_{\mathrm{S}}} \|\boldsymbol{p}_{\mathrm{H}} - \boldsymbol{G}_{\mathrm{vat}}(\boldsymbol{r}_{\mathrm{H}},\boldsymbol{r}_{\mathrm{S}})\,\boldsymbol{v}_{\mathrm{S}}\|_2^2 + \beta\|\boldsymbol{v}_{\mathrm{S}}\|_2^2, \tag{9}$$

where $\beta$ is the regularization parameter, and we use the Bayesian approach[26] to calculate the optimal value in this work. When the number of the sampling points is less than that of the pistons ($M \le N$), the general solution of Eq. (9) is expressed as

$$\boldsymbol{v}_{\mathrm{S}} = \boldsymbol{G}_{\mathrm{vat}}(\boldsymbol{r}_{\mathrm{H}},\boldsymbol{r}_{\mathrm{S}})^{\mathrm{H}}\left(\boldsymbol{G}_{\mathrm{vat}}(\boldsymbol{r}_{\mathrm{H}},\boldsymbol{r}_{\mathrm{S}})\,\boldsymbol{G}_{\mathrm{vat}}(\boldsymbol{r}_{\mathrm{H}},\boldsymbol{r}_{\mathrm{S}})^{\mathrm{H}} + \beta\boldsymbol{I}\right)^{-1}\boldsymbol{p}_{\mathrm{H}}, \tag{10}$$

where $[\cdot]^{\mathrm{H}}$ denotes the Hermitian transpose, and $\boldsymbol{I}$ is the identity matrix. Once the $\boldsymbol{v}_{\mathrm{S}}$ is obtained, the pressure $\boldsymbol{p}_{\mathrm{rec}}$ on any reconstruction surface can be calculated as

$$\boldsymbol{p}_{\mathrm{rec}} = \boldsymbol{G}_{\mathrm{vat}}(\boldsymbol{r}, \boldsymbol{r}_{\mathrm{S}})\, \boldsymbol{v}_{\mathrm{S}}, \tag{11}$$

where $\boldsymbol{p}_{\mathrm{rec}} = [p(\boldsymbol{r}_1), p(\boldsymbol{r}_2), \ldots, p(\boldsymbol{r}_N)]^{\mathrm{T}}$ is a column vector that contains the pressures on reconstructed points; $\boldsymbol{r}_n$ denotes the location of the $n$-th reconstructed point; and $\boldsymbol{G}_{\mathrm{vat}}(\boldsymbol{r}, \boldsymbol{r}_{\mathrm{S}})$ is the vibro-acoustic transfer matrix relating the pistons to the reconstructed points.

### 2.3. Compressive ERSM in sparsity framework

Suppose that the $\boldsymbol{v}_{\mathrm{S}}$ is sparse or close to being sparse, *i.e.*, a large number of the pistons make little contribution to the sound field, then some small proportion of the pistons will be enough to reconstruct the sound field. According to the CS theory, equation (7) can be solved by seeking the solution with the minimum $l_1$ norm through the minimization problem

$$\arg\min_{\boldsymbol{v}_{\mathrm{S}}} \|\boldsymbol{p}_{\mathrm{H}} - \boldsymbol{G}_{\mathrm{vat}}(\boldsymbol{r}_{\mathrm{H}}, \boldsymbol{r}_{\mathrm{S}})\, \boldsymbol{v}_{\mathrm{S}}\|_2^2 + \beta \|\boldsymbol{v}_{\mathrm{S}}\|_1. \tag{12}$$

Compared with Eq. (9), the reconstruction accuracy of Eq. (12) is higher since a more accurate prior of the signal is provided. However, a good performance of the sparse regularization relies on the suitable sparse basis and the incoherence between the transfer matrix and the sparse basis. The incoherence condition can be satisfied by using a set of randomly located microphones, and it is followed in this paper. For spatially extended sources, $\boldsymbol{v}_{\mathrm{S}}$ is generally continuous rather than sparse. Appropriate sparse basis must be introduced to decompose the $\boldsymbol{v}_{\mathrm{S}}$, and in this case the coefficient vector must be sparse. Several sparse bases have recently been suggested to cope with spatially extended sources.[24] The PRMs are combined with the source intensity instead of the normal velocity. The ARMs are used for the normal velocity, but they require the numerical integral calculation of the acoustic impedance matrix. We find that the TMMs are not only suitable for the compressive ERSM in a physical sense but also can be fast calculated via vibro-acoustic transfer matrix. Therefore, the TMMs are introduced as the sparse basis, and the reconstructed pressure TMMs are defined based on an SVD of $\boldsymbol{G}_{\mathrm{vat}}(\boldsymbol{r}, \boldsymbol{r}_{\mathrm{S}})$, specifically,

$$\boldsymbol{G}_{\mathrm{vat}}(\boldsymbol{r}, \boldsymbol{r}_{\mathrm{S}}) = \boldsymbol{U}\boldsymbol{S}\boldsymbol{V}^{\mathrm{H}} = \sum_{i=1}^{N} \boldsymbol{u}_i \sigma_i \boldsymbol{v}_i^{\mathrm{H}}, \tag{13}$$

where $\boldsymbol{U}$ and $\boldsymbol{V}$ are orthonormal matrices, their column vectors $\boldsymbol{u}_i$ and $\boldsymbol{v}_i$ are the left singular vector and the right singular vector, respectively, and $\boldsymbol{S}$ is a diagonal matrix containing singular values $\sigma_i$. Large singular values represent the low-order modes with strong radiation capability, which correspond to the low wave-number components (propagating waves). Small singular values represent the high-order modes with weak radiation capability, which correspond to the high wave-number components (evanescent waves). Right singular vectors $\boldsymbol{v}_i$ are the basis vectors that decompose the velocity $\boldsymbol{v}_{\mathrm{S}}$ to source surface, which are also named source-model modes or input TMMs; left singular vectors $\boldsymbol{u}_i$ are the basis vectors that decompose the pressure $\boldsymbol{p}_{\mathrm{rec}}$ to reconstruction mesh, namely output TMMs.[24] The output and input mode-amplitude vectors $\boldsymbol{w}_{\mathrm{out}}$ and $\boldsymbol{w}_{\mathrm{in}}$ are, respectively, expressed as

$$\boldsymbol{p}_{\mathrm{rec}} = \boldsymbol{U}\boldsymbol{w}_{\mathrm{out}}, \tag{14}$$

$$\boldsymbol{v}_{\mathrm{S}} = \boldsymbol{V}\boldsymbol{w}_{\mathrm{in}}. \tag{15}$$

The $\boldsymbol{w}_{\mathrm{out}}$ and $\boldsymbol{w}_{\mathrm{in}}$ are the coefficient vectors of $\boldsymbol{U}$ and $\boldsymbol{V}$, respectively. Combining Eqs. (11), (13), (14), and (15) gives

$$\boldsymbol{w}_{\mathrm{in}} = \boldsymbol{S}^{+}\boldsymbol{w}_{\mathrm{out}}, \tag{16}$$

where the superscript "+" denotes the pseudo-inverse. Use of Eqs. (12), (15), and (16) leads to two new optimization problems:

$$\arg\min_{\boldsymbol{w}_{\mathrm{out}}} \left\|\boldsymbol{p}_{\mathrm{H}} - \boldsymbol{G}_{\mathrm{vat}}(\boldsymbol{r}_{\mathrm{H}}, \boldsymbol{r}_{\mathrm{S}})\, \boldsymbol{V}\boldsymbol{S}^{+}\boldsymbol{w}_{\mathrm{out}}\right\|_2^2 + \beta \|\boldsymbol{w}_{\mathrm{out}}\|_1, \tag{17}$$

$$\arg\min_{\boldsymbol{w}_{\mathrm{in}}} \|\boldsymbol{p}_{\mathrm{H}} - \boldsymbol{G}_{\mathrm{vat}}(\boldsymbol{r}_{\mathrm{H}}, \boldsymbol{r}_{\mathrm{S}})\, \boldsymbol{V}\boldsymbol{w}_{\mathrm{in}}\|_2^2 + \beta \|\boldsymbol{w}_{\mathrm{in}}\|_1. \tag{18}$$

In Eq. (18), the inverse calculations are concentrated in the $l_1$ norm regularized solution, and no instability is observed in simulations. Hence, we will present the result of Eq. (18), which is equivalent to the $l_1$ norm minimization problem

$$\arg\min_{\boldsymbol{w}_{\mathrm{in}}} \|\boldsymbol{w}_{\mathrm{in}}\|_1 \ \text{subject to}$$
$$\|\boldsymbol{p}_{\mathrm{H}} - \boldsymbol{G}_{\mathrm{vat}}(\boldsymbol{r}_{\mathrm{H}}, \boldsymbol{r}_{\mathrm{S}})\, \boldsymbol{V}\boldsymbol{w}_{\mathrm{in}}\|_2^2 \le \varepsilon, \tag{19}$$

where $\varepsilon = \delta \|\boldsymbol{p}_{\mathrm{H}}\|_2$ is the data-fidelity constraint, and $\delta$ is a small number selected from $-5 \le \lg\delta < 0$. In this work, the optimal value of $\lg\delta$ is determined by a golden section search algorithm, which is an optimization technique conducted by observing the trend of an objective function.[14] Equation (19) is the basis formulation of SVD-based compressive ERSM (SVD-CERSM), which is solved by the MATLAB CVX toolbox[27] in this work. Once the coefficient vector $\boldsymbol{w}_{\mathrm{in}}$ is obtained, the $\boldsymbol{v}_{\mathrm{S}}$ is calculated via Eq. (15), and then the pressure can be reconstructed via Eq. (11).

## 3. Simulation studies

### 3.1. Validation of proposed method

This subsection will illustrate the reconstruction performance of SVD-CERSM. Taking a rectangular plate as the target source, figure 2 shows the layout of sound field reconstruction using conventional ERSM. The simply supported steel plate with dimensions of 1.0 m×0.8 m and a thickness of 3.6 mm is divided into 1600 rectangular pistons each with dimensions of 2.5 cm×2 cm. The initial microphone array is composed of 400 microphones located on a 20×20 grid (with

5 cm in interval). The reconstructions by SVD-CERSM are implemented by using a pseudo-random microphone array, in which 80 samplings are randomly selected from the initial microphone array as shown in Fig. 3. The plate is excited by a point force of 1 N in the center, and the reconstruction surface is 1 cm away from the plate. Random noise with a signal-to-noise ratio (SNR) of 40 dB is added to the measured pressures to simulate the actual measurement. The reconstruction error is defined as

$$\text{Error} = \frac{\| |\boldsymbol{p}_{\text{rec}}| - |\boldsymbol{p}_{\text{th}}| \|_2}{\|\boldsymbol{p}_{\text{th}}\|_2} \times 100\%, \tag{20}$$

where $\boldsymbol{p}_{\text{th}}$ is the theoretical pressure calculated by the Rayleigh integral. The errors from sparse sampling are averaged according to the results obtained by using ten different random microphone arrays.

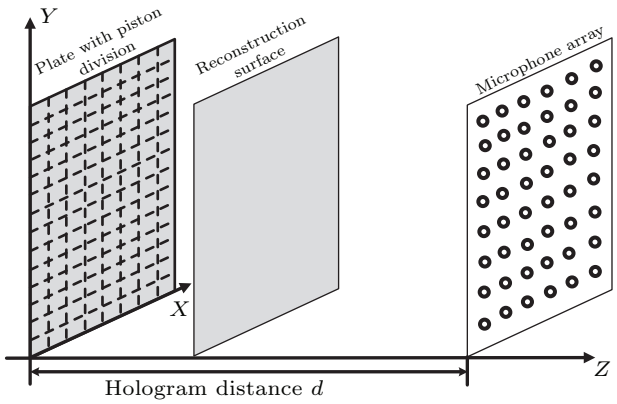



**Fig. 2.** Layout of sound field reconstruction using ERSM. Note that the assumed pistons are distributed on the plate (actual source surface).

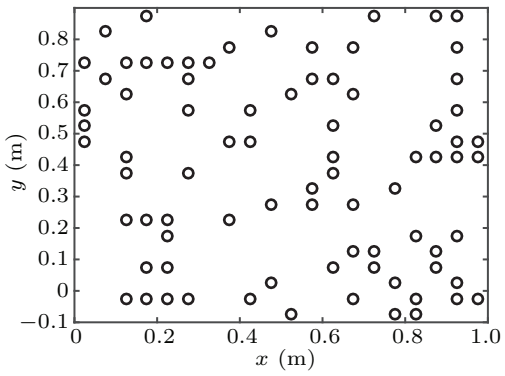



**Fig. 3.** Array with 80 randomly distributed microphones.

Firstly, the coefficient sparsity is analyzed to show whether the pressure on the reconstruction surface can be well approximated by the input TMMs. The sparse approximation is computed with the orthogonal matching pursuit (OMP) algorithm,[28] by using 10 atoms. Figure 4 shows the error of sparse approximation. It is evident that the reconstructed pressure can be well approximated by 10 atoms with the maximum error less than 5%, *i.e.*, the pressure is well approximated by using only 10 column vectors of $\boldsymbol{V}$, and in this case the coefficient vector $\boldsymbol{w}_{\text{in}}$ is definitely sparse (10 non-zero values). This indicates that the pressure is well compressed by using the input TMMs as the sparse basis.

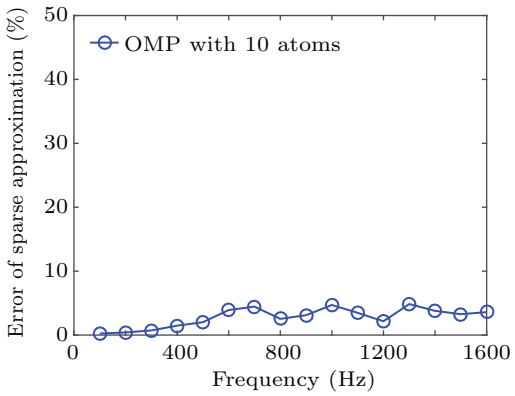



**Fig. 4.** Error of sparse approximation with input TMMs.

Figure 5 shows the reconstructed pressures using ERSM and SVD-CERSM at 800 Hz when the hologram distance $d$ is 0.15 m, 0.3 m, and 0.6 m, separately. The ERSM is implemented by using 400 and 80 sampling points, separately. The ERSM using 80 samplings gives the worst results because the insufficient sampling points cannot provide good reconstructions for conventional ERSM. In contrast, the ERSM using 400 samplings provides well reconstructions, especially at 0.15 m. The SVD-CERSM using 80 samplings also gives satisfactory results, respectively, at 0.15 m and 0.3 m, demonstrating the advantage of the proposed method. At 0.6 m, as $d$ increases distinctly, the ill-posedness in reconstruction become quite large and the high-order modes in sound field are lost; therefore, both ERSM and SVD-CERSM only reconstruct the rough sound field distribution with no detailed information.

Figure 6 shows the reconstruction errors of ERSM and SVD-CERSM from 100 Hz to 1600 Hz at three hologram distances, in which the ERSM is implemented by using 400 and 80 sampling points respectively. The reconstruction by ERSM with 80 samplings gives the worst accuracy especially at high frequencies. At 0.15 m, the reconstruction by ERSM with 400 samplings is the optimal result, and the error of SVD-CERSM is lower than 23% in the whole frequency range, indicating the good performance of SVD-CERSM with a limited samplings. At 0.3 m, the error of SVD-CERSM is almost equal to that of ERSM with 400 samplings. At 0.6 m, the high-order modes decay before reaching the microphone array and the deviations of measured data significantly increase, hence the errors of all methods become large. Even so, the error of SVD-CERSM is slightly lower than that of ERSM with 400 samplings. The reason is that the improvement by the increase of samplings is no longer obvious at a large hologram distance. This indicates the advantage of sparse regularization based on a suitable sparsity condition.

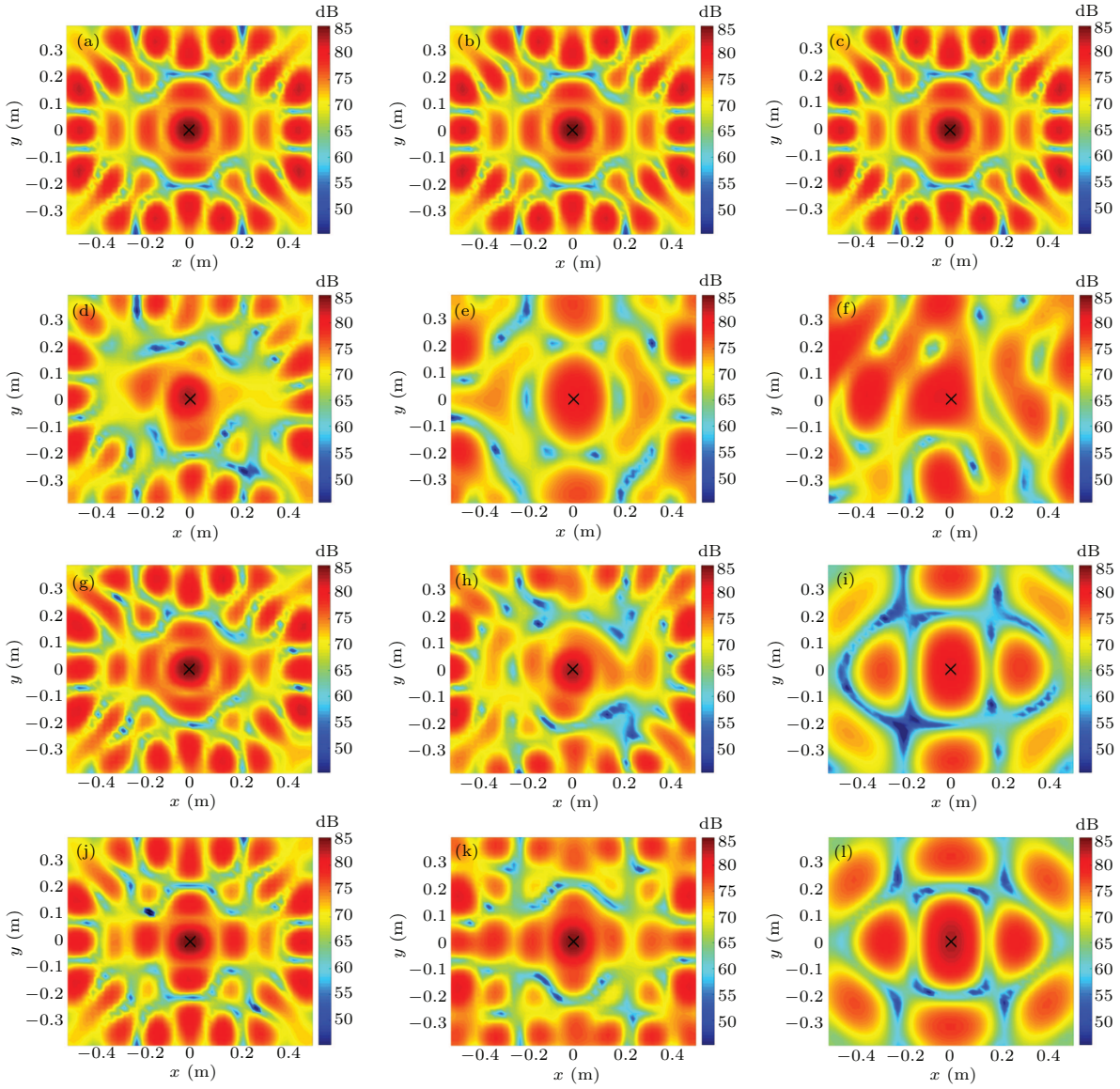



**Fig. 5.** Reconstructed pressure maps at 800 Hz from [(a)–(c)] theoretical calculation, (d) ERSM using 80 samplings when $d = 0.15$ m, (e) ERSM using 80 samplings when $d = 0.3$ m, (f) ERSM using 80 samplings when $d = 0.6$ m, (g) ERSM using 400 samplings when $d = 0.15$ m, (h) ERSM using 400 samplings when $d = 0.3$ m, (i) ERSM using 400 samplings when $d = 0.6$ m, (j) SVD-CERSM using 80 samplings when $d = 0.15$ m, (k) SVD-CERSM using 80 samplings when $d = 0.3$ m, and (l) SVD-CERSM using 80 samplings when $d = 0.6$ m.

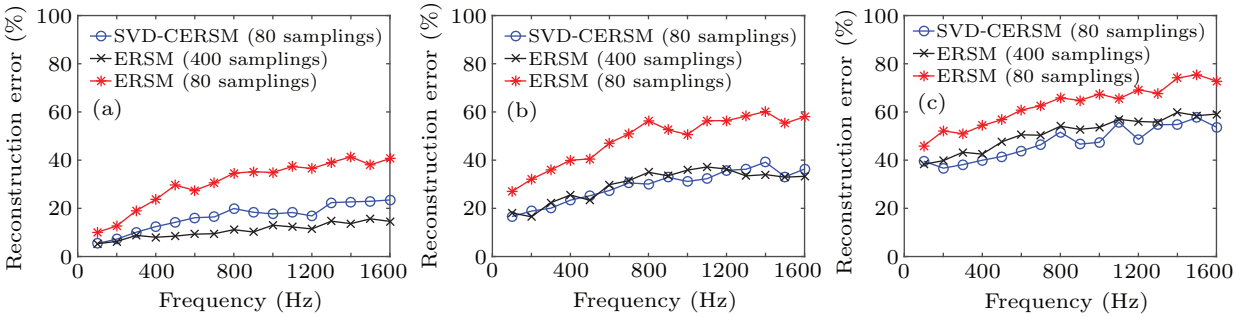



**Fig. 6.** Reconstruction errors of ERSM (full and sparse samplings) and SVD-CERSM from 100 Hz to 1600 Hz: (a) $d = 0.15$ m, (b) $d = 0.3$ m, and (c) $d = 0.6$ m.

Figure 7 shows the curves of reconstruction error of ERSM and SVD-CERSM *versus* sampling when $d = 0.15$ m. It can be seen that the error of SVD-CERSM is always lower than that of ERSM. Owing to suitable sparsity condition, the error of SVD-CERSM increases slowly with the decrease of samplings, and it is no more than 30% even with only 40 samplings. By contrast, the error of ERSM increases fast with the decrease of samplings, indicating that the conventional ERSM cannot provide an accurate reconstruction with insufficient samplings.

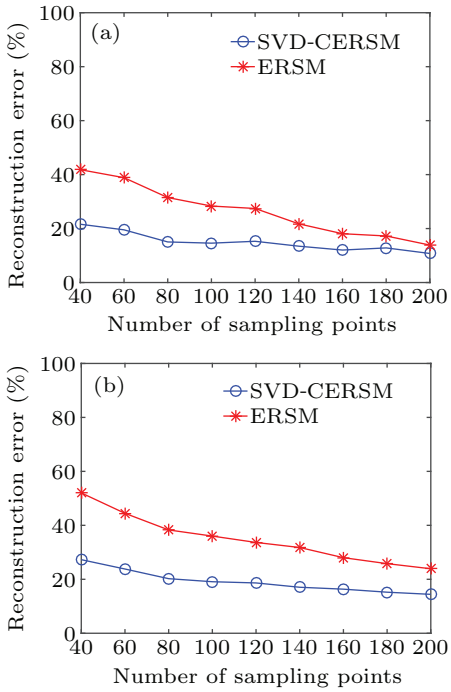



**Fig. 7.** Reconstruction errors of ERSM and SVD-CERSM *versus* number of sampling point when $d = 0.15$ m at (a) 500 Hz and (b) 1000 Hz.

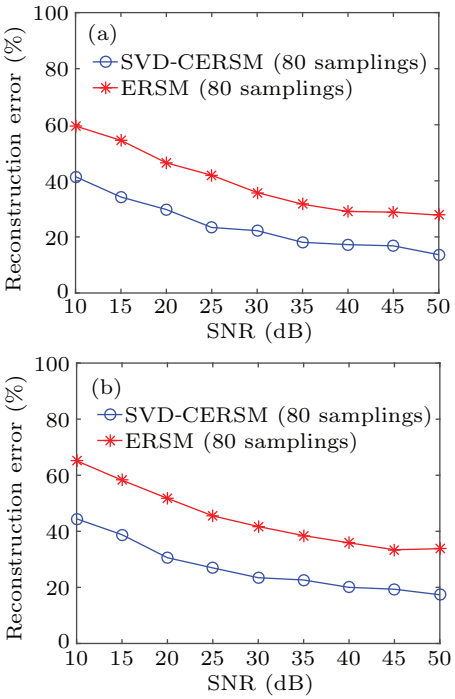



**Fig. 8.** Reconstruction errors of ERSM and SVD-CERSM *versus* SNR when $d = 0.15$ m, at (a) 500 Hz and (b) 1000 Hz.

Figure 8 shows the curves of reconstruction error *versus* SNR, in which the two methods both use 80 samplings. It can also be seen that the error of SVD-CERSM is always lower than that of ERSM. When the SNR is below 20 dB, the errors of the two methods both have an evident growth. The reconstruction is improved with SNR increasing, and the error of SVD-CERSM is below 25% when the SNR is above 30 dB, which further demonstrates the validity of the proposed method.

### 3.2. Reconstruction with less pistons

Once the $\boldsymbol{v}_S$ is represented by suitable sparse basis, the sound pressure can be well reconstructed by using some small proportion of the pistons. This subsection will compare the reconstruction accuracies of SVD-CERSM with different numbers of the pistons. The pseudo-random array is still composed of 80 microphones. The sizes of pistons are unchanged, and the initial 1600 pistons are distributed on the entire plate. The initial interval between the center points of two pistons is assumed to be $L$. Now, the interval is set to $1.5L$, $2L$, and $3L$, respectively. This leads to 625, 361, and 169 pistons accordingly. The divisions with different numbers of the pistons are shown in Fig. 9. The rest parameters in simulations are the same as those in Subsection 3.1.

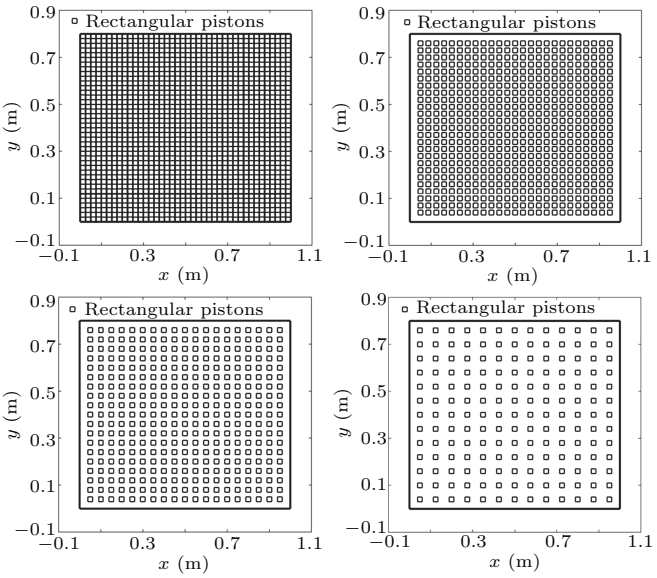



**Fig. 9.** Settings with different numbers of the pistons: (a) 1600 pistons, (b) 625 pistons, (c) 361 pistons, and (d) 169 pistons.

Figure 10 shows the reconstruction errors of SVD-CERSM with different numbers of the pistons. There is no doubt that the reconstruction of 1600 pistons in total gives the best accuracy. Though the reconstruction accuracy becomes worse with the decrease of pistons, the errors caused by using 625 and 361 pistons are only slightly higher than that using 1600 pistons, especially at low frequencies. The performance of SVD-CERSM is less dependent on the number of pistons, and the increase in pistons does not have an obvious improvement on the reconstruction. Indeed, the error caused by using 169 pistons is evidently higher than that by using more pistons since the sound field is not well represented by insufficient pistons. However, an appropriate reduction in the pistons can further enhance the calculation efficiency, which still gives an acceptable accuracy. The results at three hologram distances well indicate that the SVD-CERSM using 361 pistons is sufficient for accurate reconstruction of plate because the sparsity condition is satisfied.

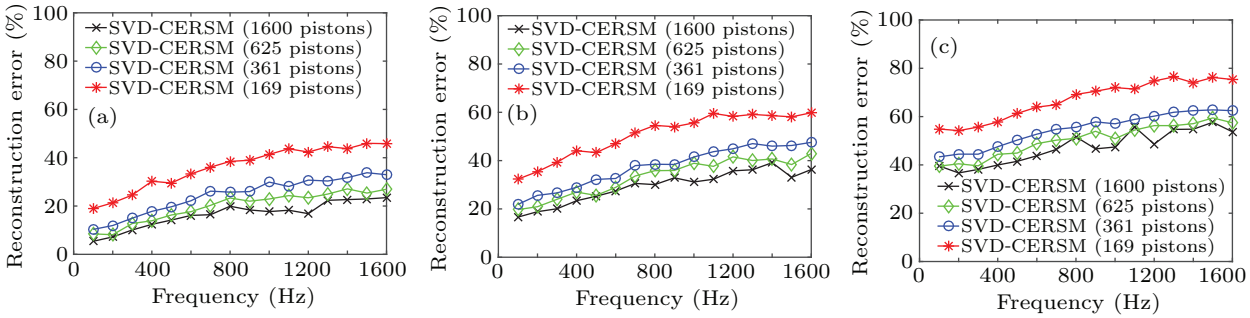



**Fig. 10.** Curves of reconstruction error *versus* frequency of SVD-CERSM with different numbers of pistons in a frequency range from 100 Hz to 1600 Hz at $d = 0.15$ m (a), 0.3 m (b), and 0.6 m (c).

### 3.3. Comparison between SVD-CERSM and SVD-CESM

As another typical reconstruction method for spatially extended sources in sparsity framework, the SVD-CESM is introduced as a benchmark in this subsection. The proposed SVD-CERSM is compared with SVD-CESM, and the differences between two methods are analyzed.

All inverse problems are mathematically ill-conditioned, and the ill-posedness difficulty is reflected in the condition number of the transfer matrix. In SVD-CERSM, the error sensitivity of $\boldsymbol{v}_{\mathrm{S}}$ is represented by

$$\frac{\|\delta \boldsymbol{v}_{\mathrm{S}}\|}{\|\boldsymbol{v}_{\mathrm{S}}\|} \leq \kappa(\boldsymbol{G}_{\mathrm{vat}}) \frac{\|\delta \boldsymbol{p}_{\mathrm{H}}\|}{\|\boldsymbol{p}_{\mathrm{H}}\|}, \tag{21}$$

where $\delta \boldsymbol{v}_{\mathrm{S}}$ is the deviation of normal velocity, $\delta \boldsymbol{p}_{\mathrm{H}}$ is the deviation of the measured data, and $\kappa(\boldsymbol{G}_{\mathrm{vat}})$ is the condition number that is the ratio of the maximum singular value to minimum singular value of $\boldsymbol{G}_{\mathrm{vat}}$. The larger the condition number, the more ill-posed the transfer matrix is and the larger the potential error. Moreover, the overlarge condition number reduces the regularized strategy and makes the acoustic quantity hard to solve. Similarly, in the SVD-CESM, the error sensitivity is written as

$$\frac{\|\delta \boldsymbol{q}\|}{\|\boldsymbol{q}\|} \leq \kappa(\boldsymbol{G}_{\mathrm{green}}) \frac{\|\delta \boldsymbol{p}_{\mathrm{H}}\|}{\|\boldsymbol{p}_{\mathrm{H}}\|}, \tag{22}$$

where $\boldsymbol{q}$ is the virtual source intensity, and $\boldsymbol{G}_{\mathrm{green}}$ is the Green's function transfer matrix. The value in $\boldsymbol{G}_{\mathrm{green}}$ is $\mathrm{j}\rho ck\mathrm{e}^{-\mathrm{j}k|\boldsymbol{r}_{\mathrm{H}}-\boldsymbol{r}_0|}/4\pi|\boldsymbol{r}_{\mathrm{H}}-\boldsymbol{r}_0|$ where $\boldsymbol{r}_0$ denotes the position of virtual sources.

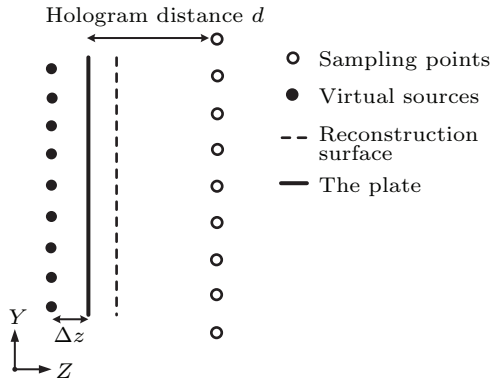



**Fig. 11.** SVD-CESM diagram. Note that the equivalent sources are retracted behind the plate (away from the reconstruction surface), to avoid their singularity being in the field.

Figure 11 shows the reconstruction by using SVD-CESM, in which the retreat distance $\Delta z$ is crucial and need to be chosen carefully. In the following simulations, the SVD-CERSM uses 361 pistons as depicted in Subsection 3.2. The SVD-CESM uses 361 virtual sources, and the locations of which coincide with the center of pistons. Both of the two methods use the pseudo-random array with 80 samplings.

In the mathematical sense, the biggest difference between the SVD-CERSM and SVD-CESM is the transfer matrix. Figure 12 shows the curves of mean condition number of the transfer matrix *versus* frequency in SVD-CERSM and SVD-CESM when ten different random arrays are used. It is evident that the condition numbers of the transfer matrix in SVD-CERSM are less than that in SVD-CESM, which means that the ill-posedness difficulty and the potential error in SVD-CERSM are less than those in SVD-CESM despite of small or large $d$. Though $\kappa(\boldsymbol{G}_{\mathrm{green}})$ decreases with the decrease of $\Delta z$, the reconstruction accuracy is not optimal at the minimal $\Delta z$ because the acoustic quantity is source intensity in SVD-CESM and the singularity should be considered. On the other hand, the overlarge $\Delta z$ increases the ill-posedness in reconstruction, which results in an increase of the potential error. Hence, an optimal $\Delta z$ is often discussed in ESM-based approaches, which may restrict the further improvement of reconstruction accuracy.

Taking the central sampling point for example, the weighting factors $\left|\boldsymbol{G}_{\mathrm{vat}}/\boldsymbol{G}_{\mathrm{green}}\right|$ ($\Delta z = 0.05$ m) at 800 Hz are shown in Fig. 13. It can be seen that the maximum value locates at the position where the center of the piston coincides with the projection of sampling point. Therefore, the off-diagonal values in $\boldsymbol{G}_{\mathrm{vat}}$ are significantly reduced, *i.e.*, the weighting of the assumed source closest to the sampling point is enhanced while the coherence of different assumed sources decreases. Compared with $\boldsymbol{G}_{\mathrm{green}}$, $\boldsymbol{G}_{\mathrm{vat}}$ is a strictly diagonally-dominant matrix, thereby guaranteeing the nonsingularity and small condition number. Meanwhile, the spatially weighting nature is weakened with the increase of $d$, and thus the difference in condition number between the two methods decreases relatively.

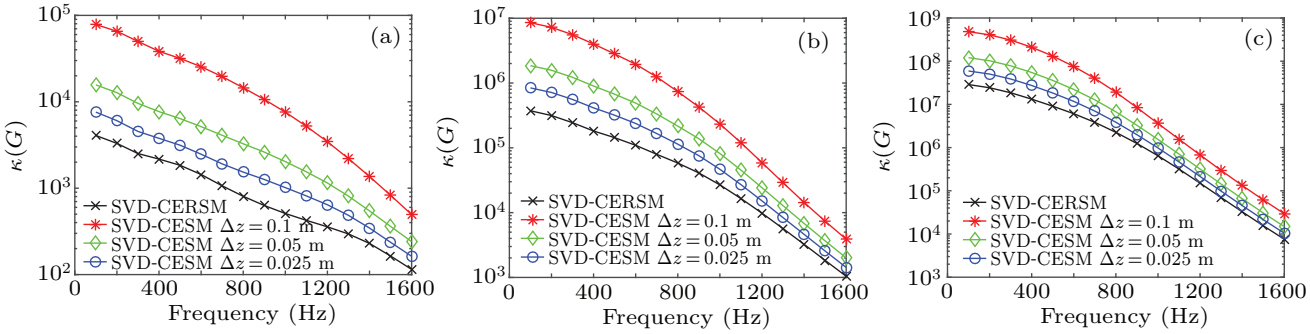



**Fig. 12.** Curves of condition numbers of transfer matrix from assumed sources to microphone array at $d = 0.15$ m (a), 0.3 m (b), and 0.6 m (c).

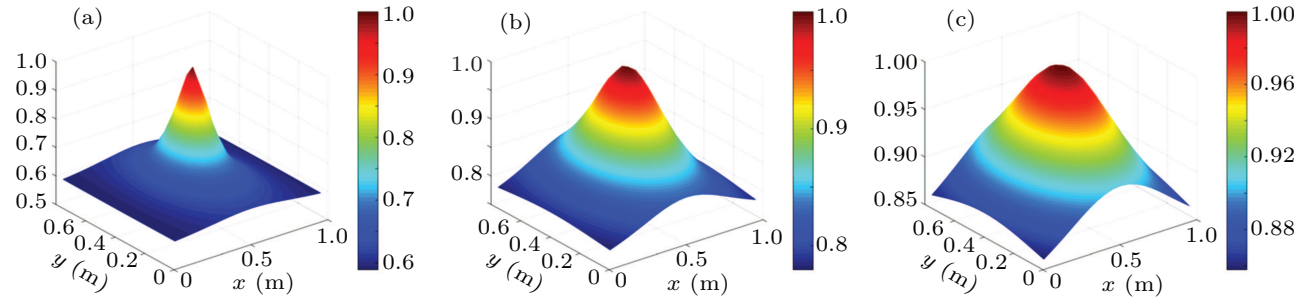



**Fig. 13.** Weighting factors $\left|\boldsymbol{G}_{\text{vat}}/\boldsymbol{G}_{\text{green}}\right|$ ($\Delta z = 0.05$ m) at 800 Hz and $d = 0.15$ m (a), 0.3 m (b), and 0.6 m (c).

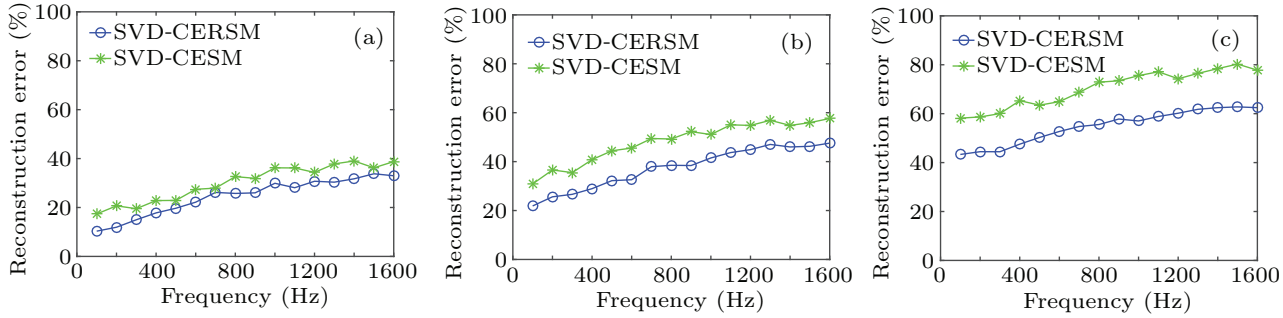



**Fig. 14.** Curves of reconstruction error *versus* frequency of SVD-CERSM and SVD-CESM ($\Delta z = 0.05$ m) in a frequency range from 100 Hz to 1600 Hz at $d = 0.15$ m (a), 0.3 m (b), and 0.6 m (c).

Figure 14 shows the curves of reconstruction error *versus* frequency for SVD-CERSM and SVD-CESM ($\Delta z = 0.05$ m). It can be seen that the errors of SVD-CERSM are always lower than those of SVD-CESM. Using the TMMs as a suitable sparse basis, both of SVD-CERSM and SVD-CESM provide an acceptable accuracy at 0.15 m, With the increase of $d$, the ill-posedness in reconstruction and the deviation in measured data become severely worse, which causes the large error-growth. The reconstructions by SVD-CERSM face relatively less ill-conditioned difficulty, and the solutions in SVD-CERSM possess weaker coherence that enhances the robustness in calculations. Consequently, the SVD-CERSM still performs better than SVD-CESM at 0.3 m and 0.6 m.

## 4. Experiment

This section describes an experiment that is carried out to evaluate the feasibility and applicability of the proposed method. The experiment is conducted in a large ordinary room in which there are environmental noise, and the experimental setup is shown in Fig. 15. A clamped steel plate with dimensions of 1.0 m×0.8 m and a thickness of 3.6 mm is used as the sound source as shown in Fig. 16(a), and this is driven in its center by a vibration exciter. A linear microphone array, which is able to slide on the rails, is used to receive the produced pressure signals as shown in Fig. 16(b). In the experiment, the total sampling points are a 19×15 grid with dimensions of 0.9 m×0.7 m and the pressures are measured on the four planes.

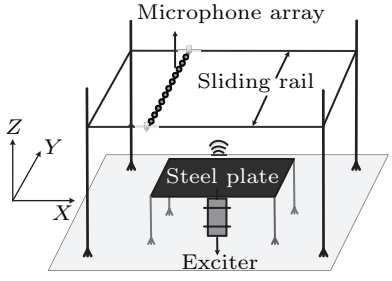



**Fig. 15.** Experimental setup.

The plane 4 cm above the plate is the reconstructed plane, on which the measured pressures are used as the theoretical values. The planes at positions 14 cm, 29 cm, and 54 cm above the plate are the hologram planes with different hologram distances. The proposed SVD-CERSM uses 40 samplings to implement the reconstruction, which are randomly selected from the original 285 sampling points. Excitation signals are generated at 100 Hz, 200 Hz, and 400 Hz, and the reconstruction errors are calculated from Eq. (20).

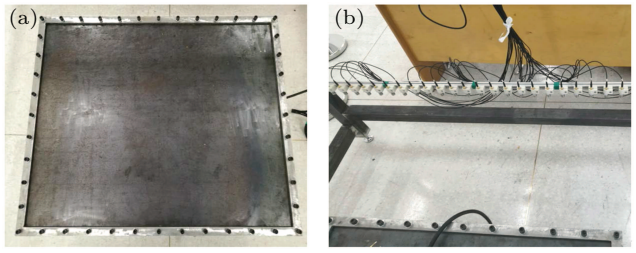



**Fig. 16.** Experimental facilities: (a) rectangular steel plate and (b) microphone array.

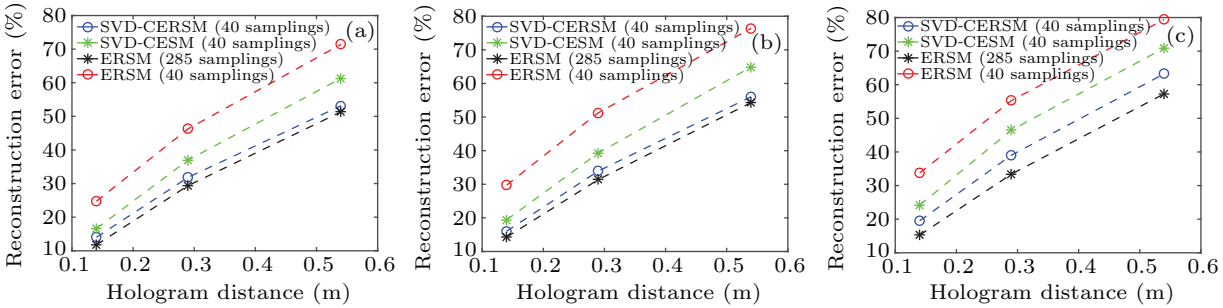



**Fig. 17.** Curves of reconstruction errors *versus* hologram distance at frequencies: (a) 100 Hz, (b) 200 Hz, and (c) 400 Hz.

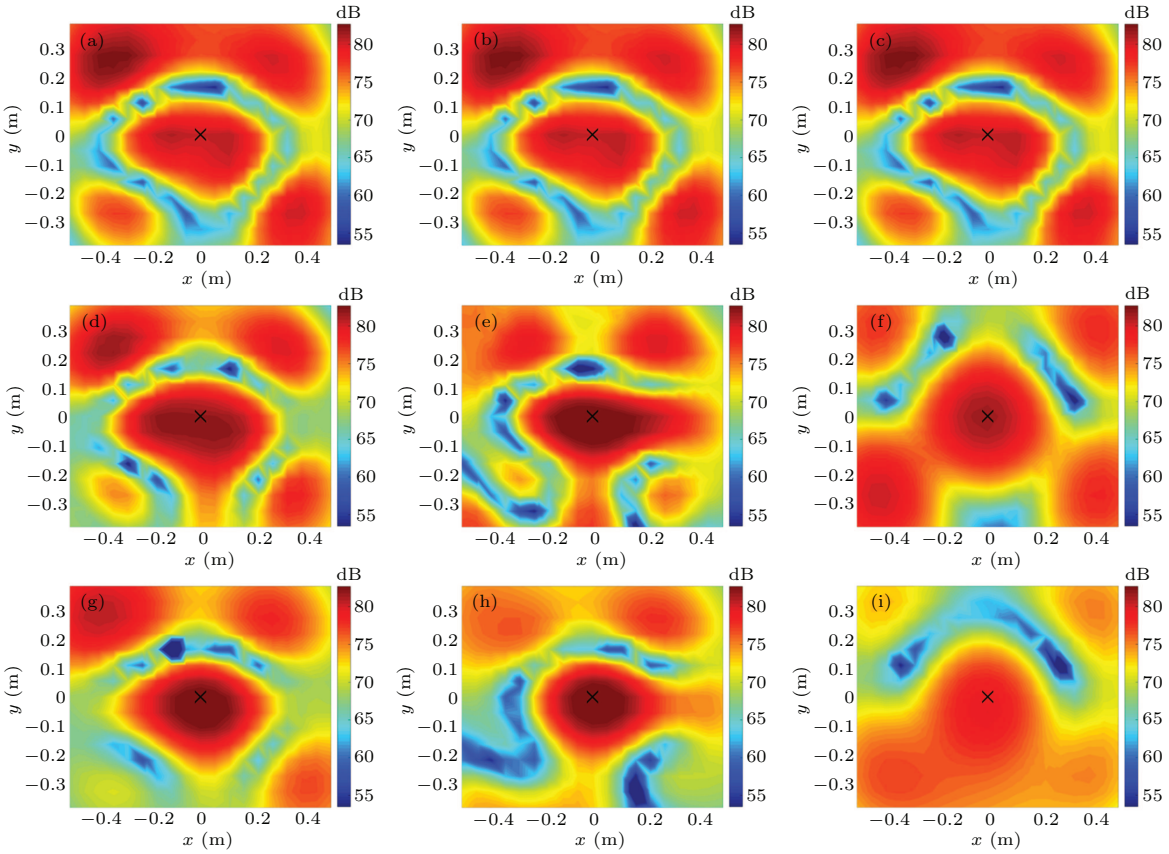



**Fig. 18.** Reconstruction maps of SVD-CERSM and SVD-CESM at 200 Hz from [(a)–(c)] theoretical results, (d) SVD-CERSM for hologram distance 0.14 m, (e) SVD-CERSM for hologram distance 0.29 m, (f) SVD-CERSM for hologram distance 0.54 m, (g) SVD-CESM for hologram distance 0.14 m, (h) SVD-CESM for hologram distance 0.29 m, and (i) SVD-CESM for hologram distance 0.54 m.

Figure 17 shows reconstruction errors at different hologram distances. The SVD-CERSM uses 361 pistons and the SVD-CESM ($\Delta z = 0.05$ m) uses 361 virtual sources. The ERSM using 1600 pistons is implemented by 285 and 40 samplings, separately. It is evident that the ERSM using 285 samplings provides the best accuracy, and the error of SVD-CERSM is slightly higher than that of ERSM using 285 samplings. There is no doubt that the ERSM using 40 samplings gives the worst accuracy because of the insufficient samplings, and the error of SVD-CESM is the second highest in the four

methods. Figure 18 shows the 2D maps reconstructed by SVD-CERSM and SVD-CESM at 200 Hz. It can be seen that the SVD-CESM performs well only at 0.14 m, while it provides less accurate reconstructions at 0.29 m and 0.54 m. By comparison, the SVD-CERSM gives better reconstructions with more sound field details at all the three hologram distances. The above results demonstrate that the proposed SVD-CERSM using less pistons can well realize the reconstruction with limited samplings.

## 5. Conclusion and perspectives

In conventional ERSM, the sizes of pistons are restricted by the application condition of far field approximation. Therefore, an accurate reconstruction requires a large number of pistons, and a large number of samplings are also needed. In this work, the TMMs, which are composed of the singular vectors of the vibro-acoustic transfer matrix, are used as the sparse basis of normal velocities of pistons. Based on this sparse basis, the sparse regularization is introduced into ERSM, and the SVD-CERSM is proposed. Simulations and experiments for a rectangular plate demonstrate that the SVD-CERSM can provide good performance with limited samplings. Meanwhile, appropriately reducing the number of the pistons, the SVD-CERSM still maintains acceptable accuracy. Compared with previous study, the number of pistons is reduced from 1600 to 361, with size unchanged. Besides, the SVD-CERSM is compared with the SVD-CESM in the mathematical sense. The ERSM-based method does not need to choose a virtual source surface as the ESM-based method. Simulations show that the transfer matrix in SVD-CERSM is a strictly diagonally-dominant matrix because it has the property of spatially weighting, which ensures its nonsingularity and the smaller condition number than the counterpart in SVD-CESM. Both simulations and experiments also indicate that the SVD-CERSM has higher accuracy than SVD-CESM in the sound field reconstruction of plate. Limited by the physical sense of ERSM, the baffled effects should be considered, and hence the ERSM-based approaches are only suitable for the spatially extended sources based on current studies. According to cylindrically and spherically curved baffled pistons, the ERSM-based approaches are expected to be applied to the reconstructions of cylindrical and spherical extended sources, and the complex structures can be processed by fitting. All the relevant studies will be conducted in the future.

## Acknowledgement

Project supported by the National Natural Science Foundation of China (Grant No. 61701133).

## References

[1] Williams E G, Maynard J D and Skudrzyk E 1980 *J. Acoust. Soc. Am.* **68** 340
[2] Wu S F 2008 *J. Acoust. Soc. Am.* **124** 2680
[3] Dong B C, Zhang R M, Yuan B and Yu C Y 2022 *Chin. Phys. B* **31** 024303
[4] Bai M R 1992 *J. Acoust. Soc. Am.* **92** 533
[5] Valdivia N P and Williams E G 2006 *J. Acoust. Soc. Am.* **120** 3694
[6] Chen M Y, Shang D J, Li Q and Liu Y W 2011 *Acta Acustica* **36** 489 (in Chinese)
[7] Koopmann G H, Song L and Fahnline J 1989 *J. Acoust. Soc. Am.* **86** 2433
[8] Zhang X Z, Bi C X, Xu L and Chen X Z 2010 *Acta Phys. Sin.* **59** 5564 (in Chinese)
[9] Wu S F and Zhao X 2002 *J. Acoust. Soc. Am.* **112** 179
[10] Semenova T and Wu S F 2005 *J. Acoust. Soc. Am.* **117** 701
[11] Sarkissian A 2005 *J. Acoust. Soc. Am.* **118** 671
[12] Zhang Y B, Bi C X, Chen J and Chen X Z 2007 *Acta Acustica* **32** 489 (in Chinese)
[13] Bi C X, Hu D Y, Zhang Y B and Xu L 2013 *Acta Phys. Sin.* **62** 084301 (in Chinese)
[14] Bai M R, Chen C C and Lin J H 2011 *J. Acoust. Soc. Am.* **129** 1407
[15] Chelliah K, Raman G G and Muehleisen R T 2016 *J. Acoust. Soc. Am.* **140** 114
[16] Wang B, Tang W L and Fan J 2008 *Acta Acustica* **33** 226 (in Chinese)
[17] Shi S G, Gao Y, Zhang H Y and Yang B Q 2021 *Acta Phys. Sin.* **70** 134301 (in Chinese)
[18] Chardon G, Daudet L, Peillot A, Ollivier F, Bertin N and Gribonval R 2012 *J. Acoust. Soc. Am.* **132** 1521
[19] Fernandez G E, Xenaki A and Gerstoft P 2017 *J. Acoust. Soc. Am.* **141** 532
[20] Fernandez G E and Daudet L 2018 *J. Acoust. Soc. Am.* **143** 3737
[21] Bi C X, Liu Y, Xu L and Zhang Y B 2017 *J. Acoust. Soc. Am.* **141** 73
[22] Bi C X, Liu Y, Zhang Y B and Xu L 2019 *J. Acoust. Soc. Am.* **145** 3154
[23] Hu D Y, Li H B, Hu Y and Fang Y 2018 *Mech. Sys. Sig. Proc.* **108** 317
[24] Hald J 2020 *J. Acoust. Soc. Am.* **147** 2211
[25] Ocheltree K B and Frizzel L A 1989 *IEEE Trans. Ultrason. Ferroelectr. Freq. Control.* **36** 242
[26] Antoni J 2012 *J. Acoust. Soc. Am.* **131** 2873
[27] Grant M and Boyd S 2011 *CVX: Matlab software for disciplined convex programming*, version 1.21 http://cvxr.com/cvx
[28] Pati Y C, Rezaiifar R and Krishnaprasad P S 1993 *Proceedings of the 27th Annual Asilomar Conference on Signals, Systems, and Computers*, November 1–3, 1993, Pacific Grove, CA, USA, p. 40